Irradiance in Mixed Coherent/Incoherent Structures: An Analytical Approach

Janez Puhan * , **Árpád Bűrmen, Tadej Tuma and Iztok Fajfar**

Faculty of Electrical Engineering, University of Ljubljana, Tržaška Cesta 25, 1000 Ljubljana, Slovenia
* Correspondence: janez.puhan@fe.uni-lj.si; Tel.: +386-1-4768-322

Abstract: We propose a new method for a light energy flux density (or irradiance) calculation in an arbitrary multilayer stack containing coherent and incoherent layers. Although the well known General Transfer-Matrix Method (GTMM) can be successfully used for the overall reflectance and transmittance calculation, it does not allow us to obtain the corresponding irradiance depth profile straightforwardly. We show in this paper that subsequent phase-shift integrations over the incoherent layers result in the reflectance and transmittance expressions identical to those of the GTMM formulation. However, the alternative mathematical approach allows us to derive an analytical expression for irradiance at an arbitrary depth of the multilayer stack, thus making it possible to calculate the absorptance depth profile. In fact, the GTMM expressions for the overall reflectance and transmittance turn out to be special cases of the irradiance calculation at the incident and emergent surface of the multilayer stack. Consequently, the proposed Phase-shift Integration Method (PIM) represents a continuous irradiance calculation model without any energy imbalances on layer interfaces. In addition, since we are able to obtain analytical layer thickness derivatives, the PIM is suitable for use with gradient optimization methods. We verify the method on three cases of an encapsulated bifacial heterojunction silicon (HJ Si) solar cell, a perovskite solar cell, and a perovskite/silicon tandem solar cell, which all consist of thin and thick layers.

Keywords: irradiance; incoherence; general transfer-matrix method; transfer-matrix formalism; multilayer; thin-film structure

1. Introduction

Thin-film multilayer structure analysis plays a key role in simulation and design of anti- and high-reflection coatings, interference thin-film optical filters, organic light-emitting diodes, and thin-film solar cells. The Transfer-Matrix Method (TMM) covered by most optical coating textbooks [1–3]—also referred to as the transfer-matrix formalism—represents the base method for reflectance, transmittance and absorptance calculation of a coherent structure (i.e., a structure consisting of an arbitrary number of isotropic, homogeneous, perfectly smooth, and parallel thin layers). A layer is considered thin (or coherent) when its thickness is well below the coherence length of light, which results in the optical interference effect. As an alternative to the TMM's 2×2 matrix formulation of coherent multilayers, the Transmission Line Method (TLM) [4,5] avoids matrices by representing a coherent multilayer structure with an equivalent chain of transmission lines.

A coherent structure of thin layers is, however, always supported by one or more thick transparent substrate layers, which lead to incoherent light propagation: the optical interference in a thick layer does not occur due to insufficient coherence length of the light (e.g., ~600 nm for sunlight [6]) and/or because of non-smooth and non-parallel interfaces of such layers. As soon as one or more thick layers are included, TMM and TLM calculations produce narrow interference fringes in reflectance/transmittance/absorptance spectra, which are physically not measurable.

Assuming finite coherence length of the incident light, the narrow spectra oscillations are smoothed out, but at the expense of an quite demanding computational procedure [7]. When a thin-film multilayer structure is supported by a single thick transparent substrate, one can still use the TMM to calculate reflectance/transmittance of the structure, as well as absorptance of a particular thin layer, provided that certain mathematical modelling is applied [8–12].

To address the incoherent layers, the TMM was upgraded into General TMM (GTMM) [13,14]. GTMM uses conventional TMM to deal with coherent layer substacks representing interfaces between the incoherent layers, and then shifts to intensity matrices to include the incoherent layers. Similarly, the TLM was upgraded into Generalized TLM (GTLM) [15]. The GTLM deals with incoherent layers one by one from the last to the first one in an iterative procedure. The last incoherent layer, including the neighboring coherent substacks, is iteratively replaced by a single equivalent interface until only one interface between the incident and emergent medium remains. One needs two TLM calculations in each replacement, representing primary and secondary reflections from the last incoherent layer.

While an absorptance calculation is not possible with GTLM, it can be done with GTMM [16], where the irradiance through a coherent/incoherent multilayer structure is calculated as a superposition of contributions of waves traveling forwards and backwards. A similar superposition approach in an absorptance calculation was used in Equivalent Matrix Method (EMM) [17]. This paper addresses the problem in a new way, using only intermediate transfer matrices.

Another set of calculation methods takes into account the actual coherence length of the incident light. Such methods can inherently deal with partially coherent layers (i.e., layers that are neither thin nor thick) which have thicknesses in the range of coherence length. Spectral Averaging Method (SAM) uses Fourier transform to convert a finite coherence length light source into a superposition of pure coherent sources, consequently producing results by superposition of coherent simulations [7]. Spectral Convolution Method (SCM), based directly on Maxwell equations, produces an incoherent response spectrum by a convolution between the incoherence function (the spectral density of the random phase switching function implementing a finite coherence length of the light source) and a coherent response spectrum [18]. Both mentioned methods use a transformation into frequency space and therefore require a substantial number of coherent calculations.

The incoherent nature of thick layers can also be covered by thickness or phase-shift averaging. In the Random Thickness Method (RTM) [19], one obtains the final result by averaging over a substantial number of coherent simulations, where one treats the incoherent layers as coherent with random thickness variations. For lossless materials, random thickness variations are equivalent to random phase-shifts, which are used in the Random Phase Method (RPM) [20]. By adjusting the size of thickness variations in RTM—or phase-shifts in RPM—both methods are also able to simulate partially coherent layers. Equispaced Thickness Averaging Method (ETAM) decreases the required number of coherent simulations [21,22], where coherent simulations are performed at fewer equispaced thickness variations instead of random ones. Similarly, the Equispaced Phase Averaging Method (EPAM) [23] uses equispaced phase-shifts. The number of coherent simulations is further reduced to only two in Phase Elimination Method (PEM) [24] by using only the first-order incoherent layer multiple reflection terms. An extension to the nth order terms and an arbitrary number of incoherent layers is presented in EMM [17].

The main advantage of averaging methods are purely coherent simulations that can be carried out using rigorous methods, such as the Finite Element Method (FEM), the Finite Difference Time Domain (FDTD), or the Rigorous Coupled Wave Analysis (RCWA). This way, the averaging procedures derived for perfectly smooth layers can be used to simulate 3D rough-surface-textured structures.

In the next section, we first briefly summarize the equations behind the TMM and GTMM. Then, in Section 3, we develop the phase-shift averaging principle, where, instead of numerical averaging, we solve the phase-shift integrals analytically. Finally, in Section 4, we verify the proposed method on three solar cell cases, and point out its potential use with gradient optimization procedures in Section 5.

2. Transfer Matrices

2.1. Coherent Structure

A coherent structure in Figure 1 is composed of n_i isotropic, homogeneous, perfectly smooth and parallel thin layers with thicknesses well below the coherence length of the incident light. Hence, we expect that the optical interference phenomena will occur in the depicted structure. We index each layer with two indexes running from $i1$ to in_i. Subscript ij represents the jth layer following the semi-infinite incident medium i denoted by subscript $i0$. The emergent medium should therefore bear subscript $i(n_i + 1)$, which we replace by subscript $(i + 1)0$. Double indexing is not really needed at this stage, but we use it to maintain a uniform indexing scheme throughout the paper.
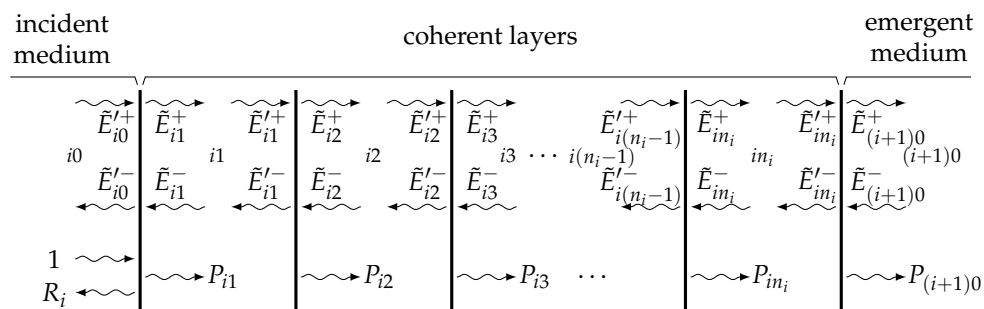
Figure 1. A coherent thin-film structure. The super- and subscripts of tangential electric field amplitudes $\tilde{E}$ denote a side of the interface, a propagation direction and a layer or medium. P is normal irradiance entering a layer at unit incident irradiance and $\tilde{E}_{(i+1)0}^- = 0$.

Beside the subscripts, the tangential components of complex electric field amplitudes $\tilde{E}$ have superscripts denoting the propagation direction and a side of an interface. Superscripts $+$ and $-$ stand for right- and left-going waves, respectively, while the prime ($'$) denotes the left side of an interface between two layers. The tilde (˜) signifies a complex nature of the tangential electric field amplitudes.

The interface conditions at the interface between arbitrary two layers are given by the relation in Equation (1), where the complex dynamical matrix $\tilde{\mathbf{D}}$ of the layer/medium ij is defined by Equation (2):

$$\tilde{\mathbf{D}}_{ij} \begin{bmatrix} \tilde{E}_{ij}'^+ \\ \tilde{E}_{ij}'^- \end{bmatrix} = \tilde{\mathbf{D}}_{i(j+1)} \begin{bmatrix} \tilde{E}_{i(j+1)}^+ \\ \tilde{E}_{i(j+1)}^- \end{bmatrix} \qquad j = 0, 1, \ldots n_i, \tag{1}$$

$$\tilde{\mathbf{D}}_{ij} = \begin{bmatrix} 1 & 1 \\ \tilde{\eta}_{ij} & -\tilde{\eta}_{ij} \end{bmatrix} \qquad j = 0, 1, \ldots n_i + 1. \tag{2}$$

Tilted refractive index of the layer/medium $\tilde{\eta}_{ij}$ is polarization dependent:

$$\tilde{\eta}_{ij} = \begin{cases} \tilde{N}_{ij} \cos \tilde{\theta}_{ij} & \text{for } s \text{ polarization} \\ \tilde{N}_{ij} / \cos \tilde{\theta}_{ij} & \text{for } p \text{ polarization} \end{cases} \qquad j = 0, 1, \ldots n_i + 1. \tag{3}$$

$\tilde{N}_{ij} = n_{ij} - \iota k_{ij}$ is the complex refractive index of the layer/medium material, and $\tilde{\theta}_{ij}$ is the complex propagation angle following Snell's law ($\tilde{N}_{i0} \sin \tilde{\theta}_{i0} = \tilde{N}_{i1} \sin \tilde{\theta}_{i1} = \ldots = \tilde{N}_{in_i} \sin \tilde{\theta}_{in_i} = \tilde{N}_{(i+1)0} \sin \tilde{\theta}_{(i+1)0}$). Although the propagation angle of the incident light might be real, the propagation angles in lossy layers or above the critical angle become complex. Nevertheless, an arbitrary tilt of the incident light is incorporated into further calculation by tilted refractive indexes. ι is the imaginary unit.

Phase-shift between the tangential field amplitudes on the left and right hand side of the layer ij is given by propagation matrix $\tilde{\mathbf{P}}_{ij}$:

$$
\begin{bmatrix} \tilde{E}_{ij}^{+} \\ \tilde{E}_{ij}^{-} \end{bmatrix} = \begin{bmatrix} e^{\iota\tilde{\delta}_{ij}} & 0 \\ 0 & e^{-\iota\tilde{\delta}_{ij}} \end{bmatrix} \begin{bmatrix} \tilde{E}_{ij}'^{+} \\ \tilde{E}_{ij}'^{-} \end{bmatrix} = \tilde{\mathbf{P}}_{ij} \begin{bmatrix} \tilde{E}_{ij}'^{+} \\ \tilde{E}_{ij}'^{-} \end{bmatrix} \qquad j = 1, 2, \ldots n_i, \tag{4}
$$

where $\tilde{\delta}_{ij} = 2\pi\tilde{N}_{ij}d_{ij}\cos\tilde{\theta}_{ij}/\lambda$ is the complex phase-shift of layer ij, d_{ij} is a layer thickness, and λ a light wavelength in free space.

Repetitive application of Equations (1) and (4) yields the relation between the input and output electric field amplitudes expressed by the complex transfer matrix $\tilde{T}_i$:

$$
\begin{bmatrix} \tilde{E}_{i0}'^{+} \\ \tilde{E}_{i0}'^{-} \end{bmatrix} = \tilde{\mathbf{D}}_{i0}^{-1}(\prod_{j=1}^{n_i} \tilde{\mathbf{D}}_{ij}\tilde{\mathbf{P}}_{ij}\tilde{\mathbf{D}}_{ij}^{-1})\tilde{\mathbf{D}}_{(i+1)0} \begin{bmatrix} \tilde{E}_{(i+1)0}^{+} \\ \tilde{E}_{(i+1)0}^{-} \end{bmatrix} = \begin{bmatrix} \tilde{T}_{i11} & \tilde{T}_{i12} \\ \tilde{T}_{i21} & \tilde{T}_{i22} \end{bmatrix} \begin{bmatrix} \tilde{E}_{(i+1)0}^{+} \\ \tilde{E}_{(i+1)0}^{-} \end{bmatrix} = \tilde{\mathbf{T}}_i \begin{bmatrix} \tilde{E}_{(i+1)0}^{+} \\ \tilde{E}_{(i+1)0}^{-} \end{bmatrix} \tag{5}
$$

Note that in the case of a single interface between the incident and emergent medium (i.e., when $n_i = 0$), the complex transfer matrix is equal to $\tilde{\mathbf{T}}_i = \tilde{\mathbf{D}}_{i0}^{-1}\tilde{\mathbf{D}}_{(i+1)0}$.

The coherent structure reflectance R_i is the ratio of the reflected normal irradiance to the input irradiance at $\tilde{E}_{(i+1)0}^{-} = 0$, and the coherent structure transmittance T_i is the ratio of the transmitted normal irradiance to the input irradiance at $\tilde{E}_{(i+1)0}^{-} = 0$. Both follow directly from Equation (5) leading to the following TMM equations:

$$
R_i = \left.\frac{|\tilde{E}_{i0}'^{-}|^2}{|\tilde{E}_{i0}'^{+}|^2}\right|_{\tilde{E}_{(i+1)0}^{-}=0} = \frac{|\tilde{T}_{i21}|^2}{|\tilde{T}_{i11}|^2} \qquad T_i = \left.\frac{\Re[\tilde{\eta}_{(i+1)0}]}{\Re[\tilde{\eta}_{i0}]}\frac{|\tilde{E}_{(i+1)0}^{+}|^2}{|\tilde{E}_{i0}'^{+}|^2}\right|_{\tilde{E}_{(i+1)0}^{-}=0} = \frac{\Re[\tilde{\eta}_{(i+1)0}]}{\Re[\tilde{\eta}_{i0}]}\frac{1}{|\tilde{T}_{i11}|^2}, \tag{6}
$$

where $\Re[\tilde{x}]$ is the real part of a complex number $\tilde{x}$. Besides R_i and T_i, normal irradiance P_{ij} entering the ijth layer normalized to incident irradiance can be expressed as:

$$
P_{ij} = \left.\frac{\Re[(\tilde{T}_{i11}^{(j)} + \tilde{T}_{i21}^{(j)})\tilde{\eta}_{i(j-1)}^{*}(\tilde{T}_{i11}^{(j)} - \tilde{T}_{i21}^{(j)})^{*}]}{\Re[\tilde{\eta}_{i0}]|\tilde{T}_{i11}|^2}\right|_{\tilde{E}_{(i+1)0}^{-}=0} \qquad j = 1, 2, \ldots n_i + 1 \tag{7}
$$

$$
\tilde{\mathbf{T}}_i^{(j)} = \begin{bmatrix} \tilde{T}_{i11}^{(j)} & \tilde{T}_{i12}^{(j)} \\ \tilde{T}_{i21}^{(j)} & \tilde{T}_{i22}^{(j)} \end{bmatrix} = \tilde{\mathbf{D}}_{i(j-1)}^{-1}(\prod_{l=j}^{n_i} \tilde{\mathbf{D}}_{il}\tilde{\mathbf{P}}_{il}\tilde{\mathbf{D}}_{il}^{-1})\tilde{\mathbf{D}}_{(i+1)0}, \tag{8}
$$

where the asterisk (*) denotes complex conjugation. Note that $T_i = P_{(i+1)0}$, and for a transparent incident medium $R_i = 1 - P_{i1}$. $\tilde{\mathbf{T}}_i^{(j)}$ is a complex transfer matrix calculated from the ijth layer onwards (Equation (8)). Note also that $\tilde{\mathbf{T}}_i^{(1)} = \tilde{\mathbf{T}}_i$.

2.2. Mixed Coherent/Incoherent Structure

A mixed coherent/incoherent structure illustrated in Figure 2 is composed of m thick layers with thicknesses well above the coherence length of the incident light. Hence, the optical interference phenomenon in those layers does not occur. Thick (i.e., incoherent) layers are indexed using subscripts from 10 to $m0$. The semi-infinite incident medium bears subscript 00, and the semi-infinite emergent medium is indexed $(m + 1)0$. Between every $i0$th and $(i + 1)0$th incoherent layer/medium, there are n_i coherent layers, as depicted in Figure 1. Those coherent layer stacks represent interfaces between incoherent layers.

Equation (5) describes the ith coherent stack and can be rearranged into:

$$
\begin{bmatrix} \tilde{E}_{(i+1)0}^{+} \\ \tilde{E}_{i0}'^{-} \end{bmatrix} = \frac{1}{\tilde{T}_{i11}} \begin{bmatrix} 1 & -\tilde{T}_{i12} \\ \tilde{T}_{i21} & \det\tilde{T}_i \end{bmatrix} \begin{bmatrix} \tilde{E}_{i0}'^{+} \\ \tilde{E}_{(i+1)0}^{-} \end{bmatrix} \qquad i = 0, 1, \ldots m. \tag{9}
$$

Considering $\tilde{E}'^{+}_{i0}$ and $\tilde{E}^{-}_{(i+1)0}$ as two independent waves hitting the coherent structure in Figure 1 from the left and right, respectively, the rearranged Equation (9) can be absolute squared for each of the waves separately:

$$
\begin{bmatrix} |\tilde{E}^{+}_{(i+1)0}|^2 \\ |\tilde{E}'^{-}_{i0}|^2 \end{bmatrix} = \frac{1}{|\tilde{T}_{i11}|^2} \begin{bmatrix} 1 & |\tilde{T}_{i12}|^2 \\ |\tilde{T}_{i21}|^2 & |\det \tilde{T}_i|^2 \end{bmatrix} \begin{bmatrix} |\tilde{E}'^{+}_{i0}|^2 \\ |\tilde{E}^{-}_{(i+1)0}|^2 \end{bmatrix} \qquad i = 0, 1, \dots m. \tag{10}
$$

Rearranging Equation (10) back to its original form, the relation among squared absolutes of tangential components of complex electric field amplitudes for a coherent structure is obtained as:

$$
\begin{bmatrix} |\tilde{E}'^{+}_{i0}|^2 \\ |\tilde{E}'^{-}_{i0}|^2 \end{bmatrix} = \begin{bmatrix} |\tilde{T}_{i11}|^2 & -|\tilde{T}_{i12}|^2 \\ |\tilde{T}_{i21}|^2 & \frac{|\det \tilde{T}_i|^2 - |\tilde{T}_{i12}|^2 |\tilde{T}_{i21}|^2}{|\tilde{T}_{i11}|^2} \end{bmatrix} \begin{bmatrix} |\tilde{E}^{+}_{(i+1)0}|^2 \\ |\tilde{E}^{-}_{(i+1)0}|^2 \end{bmatrix} = \mathbf{J}_i \begin{bmatrix} |\tilde{E}^{+}_{(i+1)0}|^2 \\ |\tilde{E}^{-}_{(i+1)0}|^2 \end{bmatrix} \qquad i = 0, 1, \dots m. \tag{11}
$$

Note that intensity matrix $\mathbf{J}_i$ is a real-valued matrix.
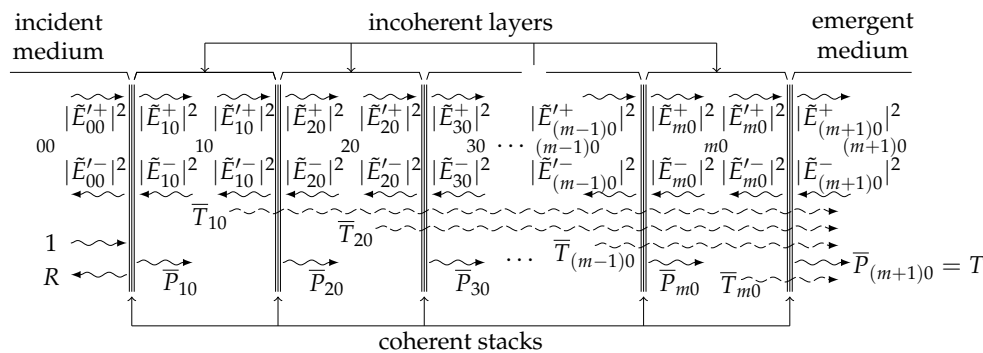
Figure 2. A mixed coherent/incoherent structure. The coherent thin-film stacks represent interfaces between incoherent layers including the incident and emergent media. $\overline{P}_{i0}$ is normal irradiance entering incoherent layer $i0$. $\overline{T}_{i0} = \overline{P}_{(m+1)0}/\overline{P}'^{+}_{i0}$ is the transmittance from incoherent layer $i0$ towards the emergent medium $(m + 1)0$. $\overline{P}'^{+}_{i0}$ is the irradiance caused by the right-going wave $\tilde{E}'^{+}_{i0}$.

Since phase information is lost in an incoherent layer, only its non-transparency can be established by absolute ratio of tangential filed amplitudes. The relation between the left and right hand side absolute values in an incoherent layer $i0$ is given by intensity propagation matrix $\mathbf{P}_i$:

$$
\begin{bmatrix} |\tilde{E}^{+}_{i0}|^2 \\ |\tilde{E}^{-}_{i0}|^2 \end{bmatrix} = \begin{bmatrix} |e^{\iota \tilde{\delta}_{i0}}|^2 & 0 \\ 0 & |e^{-\iota \tilde{\delta}_{i0}}|^2 \end{bmatrix} \begin{bmatrix} |\tilde{E}'^{+}_{i0}|^2 \\ |\tilde{E}'^{-}_{i0}|^2 \end{bmatrix} = \mathbf{P}_i \begin{bmatrix} |\tilde{E}'^{+}_{i0}|^2 \\ |\tilde{E}'^{-}_{i0}|^2 \end{bmatrix} \qquad i = 1, 2, \dots m. \tag{12}
$$

Note that $\mathbf{P}_i$ is real, and that, for a transparent incoherent layer, it reduces into a unity matrix.

Repetitive application of Equations (11) and (12) yields the relation between the squared input and output absolute values of tangential electric field amplitudes expressed by the intensity transfer matrix $\mathbf{T}$:

$$
\begin{bmatrix} |\tilde{E}'^{+}_{00}|^2 \\ |\tilde{E}'^{-}_{00}|^2 \end{bmatrix} = \mathbf{J}_0 \prod_{i=1}^{m} (\mathbf{P}_i \mathbf{J}_i) \begin{bmatrix} |\tilde{E}^{+}_{(m+1)0}|^2 \\ |\tilde{E}^{-}_{(m+1)0}|^2 \end{bmatrix} = \begin{bmatrix} T_{11} & T_{12} \\ T_{21} & T_{22} \end{bmatrix} \begin{bmatrix} |\tilde{E}^{+}_{(m+1)0}|^2 \\ |\tilde{E}^{-}_{(m+1)0}|^2 \end{bmatrix} = \mathbf{T} \begin{bmatrix} |\tilde{E}^{+}_{(m+1)0}|^2 \\ |\tilde{E}^{-}_{(m+1)0}|^2 \end{bmatrix}. \tag{13}
$$

Apparently, intensity transfer matrix $\mathbf{T}$ is a real-valued matrix.

The overall reflectance/transmittance is the ratio of the reflected/transmitted irradiance to the input irradiance at $\tilde{E}^{-}_{(m+1)0} = 0$. Both follow directly from Equation (13). Finally, we arrive to the following GTMM equations:

$$R = \frac{|\tilde{E}_{00}'^-|^2}{|\tilde{E}_{00}'^+|^2}\Bigg|_{\tilde{E}_{(m+1)0}^-=0} = \frac{T_{21}}{T_{11}} \qquad T = \frac{\Re[\tilde{\eta}_{(m+1)0}]}{\Re[\tilde{\eta}_{00}]}\frac{|\tilde{E}_{(m+1)0}^+|^2}{|\tilde{E}_{00}'^+|^2}\Bigg|_{\tilde{E}_{(m+1)0}^-=0} = \frac{\Re[\tilde{\eta}_{(m+1)0}]}{\Re[\tilde{\eta}_{00}]}\frac{1}{T_{11}}. \quad (14)$$

3. Phase-Shift Integration

In this section, we develop and explain our phase-shift averaging principle, where we replace the usual numerical averaging with an analytical integration.

3.1. Theory

With the introduction of incoherent layers in Figure 2, we cannot use Equation (7) to calculate normalized normal irradiance entering an arbitrary layer. If all the layers in Figure 2 are coherent, then the complex transfer matrix $\tilde{\mathbf{T}}^{(ij)}$ from the *ij*th layer onwards transforms from Equation (8) into:

$$\tilde{\mathbf{T}}^{(ij)} = \tilde{\mathbf{T}}_i^{(j)}\tilde{\mathbf{P}}_{(i+1)0}\tilde{\mathbf{T}}_{i+1}\prod_{l=i+2}^{m}\tilde{\mathbf{P}}_{l0}\tilde{\mathbf{T}}_l = \tilde{\mathbf{T}}_i^{(j)}\tilde{\mathbf{P}}_{(i+1)0}\tilde{\mathbf{T}}^{((i+1)1)} \quad (15)$$

$$\tilde{T}_{11}^{(ij)} = \tilde{T}_{i11}^{(j)}e^{\iota\tilde{\delta}_{(i+1)0}}\tilde{T}_{11}^{((i+1)1)} + \tilde{T}_{i12}^{(j)}e^{-\iota\tilde{\delta}_{(i+1)0}}\tilde{T}_{21}^{((i+1)1)} = \frac{\tilde{T}_{i11}^{(j)}e^{\iota\tilde{\delta}_{(i+1)0}} + \tilde{T}_{i12}^{(j)}e^{-\iota\tilde{\delta}_{(i+1)0}}\tilde{r}_{(i+1)0}}{\tilde{t}_{(i+1)0}} \quad (16)$$

$$\tilde{T}_{21}^{(ij)} = \tilde{T}_{i21}^{(j)}e^{\iota\tilde{\delta}_{(i+1)0}}\tilde{T}_{11}^{((i+1)1)} + \tilde{T}_{i22}^{(j)}e^{-\iota\tilde{\delta}_{(i+1)0}}\tilde{T}_{21}^{((i+1)1)} = \frac{\tilde{T}_{i21}^{(j)}e^{\iota\tilde{\delta}_{(i+1)0}} + \tilde{T}_{i22}^{(j)}e^{-\iota\tilde{\delta}_{(i+1)0}}\tilde{r}_{(i+1)0}}{\tilde{t}_{(i+1)0}} \quad (17)$$

$$\tilde{r}_{(i+1)0} = \frac{\tilde{T}_{21}^{((i+1)1)}}{\tilde{T}_{11}^{((i+1)1)}} \qquad \tilde{t}_{(i+1)0} = \frac{1}{\tilde{T}_{11}^{((i+1)1)}} \qquad i = 0, 1, \ldots m-1 \qquad j = 1, 2, \ldots n_i + 1.$$

We can obtain transmittance T_{i0} from the *i*0th layer towards the emergent medium, and normal irradiance P_{ij} entering the *ij*th layer, by replacing Equations (16) and (17) in TMM (Equations (6) and (7)). Thus:

$$T_{i0} = \frac{\Re[\tilde{\eta}_{(m+1)0}]}{\Re[\tilde{\eta}_{i0}]}\frac{1}{|\tilde{T}_{i11}^{(i1)}|^2} \qquad P_{ij} = \frac{\Re[(\tilde{T}_{11}^{(ij)} + \tilde{T}_{21}^{(ij)})\tilde{\eta}_{i(j-1)}^*(\tilde{T}_{11}^{(ij)} - \tilde{T}_{21}^{(ij)})^*]}{\Re[\tilde{\eta}_{i0}]|\tilde{T}_{11}^{(i1)}|^2} \quad (18)$$

$$i = 0, 1, \ldots m-1 \qquad j = 1, 2, \ldots n_i + 1.$$

Note that Equation (18) is valid only when all the layers are coherent. T_{i0} and P_{ij} depend on phase-shift $\tilde{\delta}_{(i+1)0}$ of the layer $(i+1)0$ and the reflection and transmission coefficients $\tilde{r}_{(i+1)0}$ and $\tilde{t}_{(i+1)0}$ of the layer $(i+1)0$ towards the emergent medium. They are both periodic functions of the phase-shift's real part $\Re[\tilde{\delta}_{(i+1)0}]$ with a period π. If, however, layer $(i+1)0$ is incoherent, we have to calculate the average by the phase $\Re[\tilde{\delta}_{(i+1)0}]$:

$$\overline{T}_{i0} = \frac{1}{\pi}\int_{-\frac{\pi}{2}}^{\frac{\pi}{2}}T_{i0}\mathrm{d}\Re[\tilde{\delta}_{(i+1)0}] \qquad \overline{P}_{ij} = \frac{1}{\pi}\int_{-\frac{\pi}{2}}^{\frac{\pi}{2}}P_{ij}\mathrm{d}\Re[\tilde{\delta}_{(i+1)0}] \quad (19)$$

$$i = 0, 1, \ldots m-1 \qquad j = 1, 2, \ldots n_i + 1.$$

We can solve the integrals in Equation (19) analytically (see Appendix A for detailed integration procedure), thus obtaining the following PIM equations:

$$\overline{T}_{i0} = \frac{\Re[\tilde{\eta}_{(i+1)0}]\overline{T}_{(i+1)0}e^{2\Im[\tilde{\delta}_{(i+1)0}]}}{\Re[\tilde{\eta}_{i0}](|\tilde{T}_{i11}|^2 - |\tilde{T}_{i12}|^2(1 - \overline{P}_{(i+1)1\Re})e^{4\Im[\tilde{\delta}_{(i+1)0}]})} \tag{20}$$

$$\overline{P}_{ij} = \overline{P}_{ij\Re} + \overline{P}_{ij\Im} \tag{21}$$

$$\overline{P}_{ij\Re} = \frac{\Re[\tilde{\eta}_{i(j-1)}](|\tilde{T}_{i11}^{(j)}|^2 - |\tilde{T}_{i21}^{(j)}|^2 + c_i^{(j)}(1 - \overline{P}_{(i+1)1\Re})e^{4\Im[\tilde{\delta}_{(i+1)0}]})}{\Re[\tilde{\eta}_{i0}](|\tilde{T}_{i11}|^2 - |\tilde{T}_{i12}|^2(1 - \overline{P}_{(i+1)1\Re})e^{4\Im[\tilde{\delta}_{(i+1)0}]})} \tag{22}$$

$$\overline{P}_{ij\Im} = \frac{2\Im[\tilde{\eta}_{i(j-1)}]\Im[\tilde{T}_{i11}^{(j)*}\tilde{T}_{i21}^{(j)} + (\tilde{T}_{i12}^{(j)*}\tilde{T}_{i22}^{(j)} - \frac{\tilde{T}_{i11}^*\tilde{T}_{i12}(\tilde{T}_{i12}^{(j)*}\tilde{T}_{i21}^{(j)} - \tilde{T}_{i11}^{(j)}\tilde{T}_{i22}^{(j)*})}{|\tilde{T}_{i11}|^2})(1 - \overline{P}_{(i+1)1\Re})e^{4\Im[\tilde{\delta}_{(i+1)0}]}]}{\Re[\tilde{\eta}_{i0}](|\tilde{T}_{i11}|^2 - |\tilde{T}_{i12}|^2(1 - \overline{P}_{(i+1)1\Re})e^{4\Im[\tilde{\delta}_{(i+1)0}]})} \tag{23}$$

$$c_i^{(j)} = \frac{|\tilde{T}_{i11}\tilde{T}_{i12}^{(j)} - \tilde{T}_{i12}\tilde{T}_{i11}^{(j)}|^2 - |\tilde{T}_{i11}\tilde{T}_{i22}^{(j)} - \tilde{T}_{i12}\tilde{T}_{i21}^{(j)}|^2 - |\tilde{T}_{i12}|^2(|\tilde{T}_{i11}^{(j)}|^2 - |\tilde{T}_{i21}^{(j)}|^2)}{|\tilde{T}_{i11}|^2}$$

$$i = 0, 1, \dots m - 1 \qquad j = 1, 2, \dots n_i + 1,$$

where $\Im[\tilde{x}]$ is the imaginary part of a complex number $\tilde{x}$.

We obtain Equations (20)–(23) by averaging the $(i + 1)0$th layer phase, thus capturing its incoherent nature. The incoherent nature of the subsequent layers $(i + 2)0, (i + 3)0, \dots, m0$ is taken into account by the average reflectance $\overline{R}_{(i+1)0} = 1 - \overline{P}_{(i+1)1\Re}$ and transmittance $\overline{T}_{(i+1)0}$ of the $(i + 1)0$th layer towards the emergent medium.

Note that Equations (20)–(23) allow us to calculate only the irradiance entering a particular layer. To calculate irradiance at an arbitrary depth of the multilayer stack, we have to add a virtual boundary at the desired depth, dividing the corresponding layer into two layers of the same material and nature.

Since the irradiances are not calculated directly from the squared electric field amplitudes of the waves traveling forwards and backwards in an individual incoherent layer, there is no energy imbalance error caused by wave coupling when the layer is lossy. Energy conservation law is preserved throughout the structure. For instance, by inserting a zero thickness virtual needle layer anywhere in the structure, nothing changes since the needle has no impact. To preserve the conservation law, the irradiances entering the needle and the subsequent layer must be equal. Since the complex transfer matrix of the needle $\tilde{\mathbf{T}}_{needle}$ is a real unity matrix, Equations (20)–(23) confirm that. The irradiance depth profile of the structure is therefore continuous.

3.2. PIM Algorithm

For solving Equations (20)–(23), we devised an algorithm, as outlined in Algorithm 1. First, we calculate all the complex transfer matrices $\tilde{\mathbf{T}}_i^{(j)}$. To simplify the algorithm, we then introduce a virtual boundary by adding a zero-width layer of the same composition as the emergent medium just before the emergent medium. Thus, the added layer obtains index $(m + 1)0$, while the existing emergent medium obtains index $(m + 2)0$. This manipulation simplifies the algorithm, as we can also use Equations (20)–(23) for the last coherent stack with indexes from $m1$ to $m(n_m + 1)$ (which is equivalent to indexes from $m1$ to $(m + 1)0$). The core of the algorithm calculates the layer entering irradiances $\overline{P}_{ij}$ that are normalized to the emergent transmittance $\overline{T}_{i0}$. Normalization is essential since the irradiances have to be calculated backwards from the last layer to the first. Finally, we renormalize the calculated irradiances to the incident irradiance. At the conclusion of the algorithm, we calculate the overall reflectance R.

Algorithm 1 PIM algorithm

1: ▷ Calculate all the matrices $\tilde{\mathbf{T}}_i^{(j)}$ using Equation (8)

2: **for** $i \leftarrow 0$ **to** m **do**

3:      $\tilde{\mathbf{T}}_i^{(n_i+1)} \leftarrow \tilde{\mathbf{D}}_{in_i}^{-1} \tilde{\mathbf{D}}_{(i+1)0}$

4:      **for** $j \leftarrow n_i$ **to** 1 **do**

5:          $\tilde{\mathbf{T}}_i^{(j)} \leftarrow \tilde{\mathbf{D}}_{i(j-1)}^{-1} \tilde{\mathbf{D}}_{ij} \tilde{\mathbf{P}}_{ij} \tilde{\mathbf{T}}_i^{(j+1)}$

6:      **end for**

7: **end for**

8: ▷ Transform emergent medium into zero length incoherent layer $(m+1)0$

9: $\tilde{\delta}_{(m+1)0} \leftarrow 0, \quad \overline{T}_{(m+1)0} \leftarrow 1, \quad \overline{P}_{(m+1)1\Re} \leftarrow 1$

10: ▷ Calculate layer entering irradiances Q_{ij} normalized to the emergent irradiance

11: **for** $i \leftarrow m$ **to** 0 **do**

12:      Calculate and save $\overline{T}_{i0}$ and $\overline{P}_{i1\Re}$ for the next iteration, use Equations (20) and (22)

13:      **for** $j \leftarrow 1$ **to** n_i+1 **do**   ▷ Note that index $i(n_i+1)$ is equivalent to index $(i+1)0$

14:          $Q_{ij} \leftarrow \dfrac{\overline{P}_{ij}}{\overline{T}_{i0}}$, use Equations (21)–(23)

15:      **end for**

16: **end for**

17: ▷ Renormalize layer entering irradiances to the incident irradiance

18: **for** $i \leftarrow m$ **to** 0 **do**

19:      **for** $j \leftarrow 1$ **to** n_i+1 **do**   ▷ Note that index $i(n_i+1)$ is equivalent to index $(i+1)0$

20:          $\overline{P}_{ij} \leftarrow Q_{ij}\overline{T}_{00}$

21:      **end for**

22: **end for**

23: ▷ Calculate overall reflectance R

24: $R \leftarrow 1 - \overline{P}_{01\Re}$

The above PIM algorithm is actually a generalized GTMM algorithm. By removing Lines 13–15, and replacing Lines 17–22 with $T \leftarrow \overline{T}_{00}$, the PIM algorithm transforms into an algorithm that is mathematically identical to the GTMM algorithm. The removed **for** loops perform the calculation of the internal layer entering irradiances, which is not included in the GTMM.

4. Verification Cases

The proposed PIM is a matrix based method that operates with isotropic, homogeneous, perfectly smooth and parallel layers. Since the performance improving surface-textures are not included, the PIM results are not in perfect match with realistic structures. However, since PIM is a generalization of the GTMM, the methods' performances are exactly the same. Although PIM does not address surface-textures, it is quick, analytical and analytically derivable (see Section 5), which makes it interesting in gradient layer thickness optimization procedures. The PIM results in the verification cases were compared with GTMM (overall reflectance and transmittance only) and the Combined Ray Optics/Wave optics Model (CROWM) [25]. The PIM and GTMM results are, as expected, always identical, while CROWM results slightly differ. The CROWM simulator produces results to eight decimal places, although the last few are physically insignificant. Nevertheless, the PIM results always agree with CROWM's to at least four decimal places ($|\text{PIM} - \text{CROWM}| < 10^{-4}$), although the numerical procedures used in either method are completely different.

4.1. Encapsulated Bifacial Heterojunction Silicon Solar Cell

The first verification case is an encapsulated bifacial heterojunction silicon (HJ Si) solar cell [26,27]. The structure of the HJ Si cell that we use is shown in Figure 3. It consists of five thick incoherent, and six thin coherent layers. The structure is enclosed in front and rear coverings of glass (3.2 mm) and ethylene-vinyl acetate (EVA, 500 μm), which represent four thick layers that were included in the simulation. The solar cell itself consists of thin layers of conductive indium tin oxide (ITO, 119 nm), n-type hydrogenated amorphous silicon (n-a-Si:H, 10.2 nm), and intrinsic hydrogenated amorphous silicon (i-a-Si:H, 13.6 nm) in front of a thick crystalline silicon (c-Si) absorber (200 μm), and thin layers of i-a-Si:H (13.6 nm), p-type hydrogenated amorphous silicon (p-a-Si:H, 18.6 nm), and ITO (204 nm) at the back. We obtained the complex refractive indexes of the used materials from the PhotoVoltaic Lighthouse refractive index database [28].
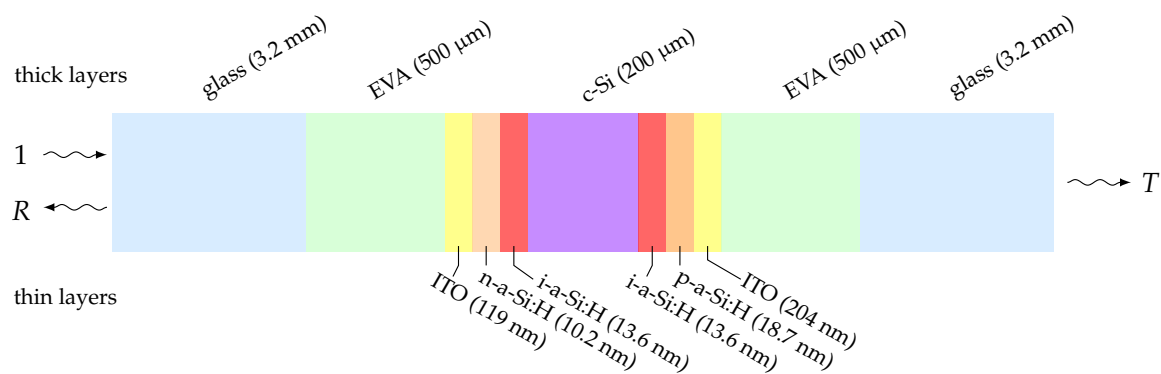

Figure 3. Encapsulated bifacial HJ Si solar cell multilayer structure.

The graphs in Figure 4 show PIM calculated wavelength dependent layer absorptances of the encapsulated bifacial HJ Si solar cell from Figure 3. The curves represent the normalized irradiances entering individual layers. Hence, a normalized layer absorptance is the difference between the two neighboring curves representing the irradiances entering one particular layer and the following one. The topmost curve is the normalized irradiance entering the structure (i.e., the incident irradinace decreased by the overall reflectance R), and the bottommost curve is the normalized irradiance leaving the structure (i.e., the overall transmittance T). The graphs show the absorption distribution as anticipated from the used HJ Si solar cell structure. The ultraviolet light is absorbed in the glass and EVA layers and the c-Si absorber layer absorbs the major part of the visible and some of the infrared light ($A_{\text{c-Si}}$). On the other hand, the structure is fairly non-absorptive for wavelengths above 1 μm.
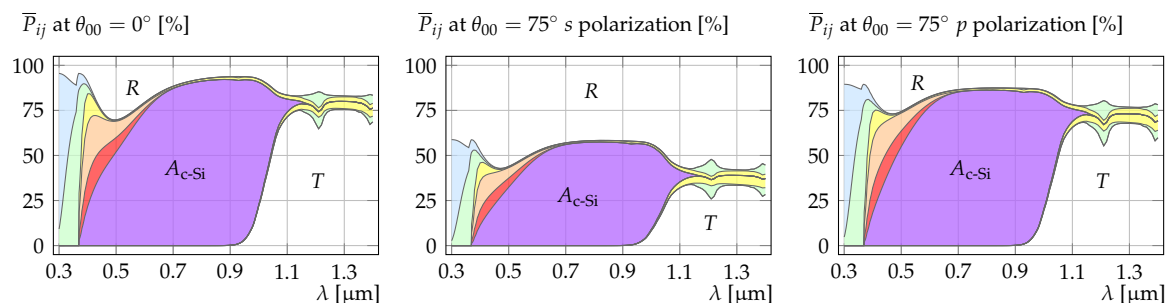

Figure 4. Wavelength dependent layer absorptances of the encapsulated bifacial HJ Si solar cell at the specified incident angles and polarizations. The height of a particular colored area (refer to Figure 3 for the meaning of the colors) represents the corresponding layer's absorptance as a function of wavelength. The white area above (up to 100%) represents the overall reflectance R, and below (down to 0%) the overall transmittance T.

The PIM calculated irradiance depth profiles of the used HJ Si solar structure are shown in Figure 5. We divided each layer into ten equivalent sublayers, thus obtaining a structure of 110 layers for calculation (50 of which were treated as thick, and the rest as thin). Beside the actual interfaces dividing adjacent layers, we added nine equispaced virtual interfaces into each layer. Accordingly, the irradiances calculated at those virtual interfaces produce irradiance values at various depths within each individual layer, thus creating a depth profile. The irradiances at actual interfaces (marked by vertical grid lines in Figure 5) are identical to the ones that can be obtained from Figure 4 for the same wavelengths.
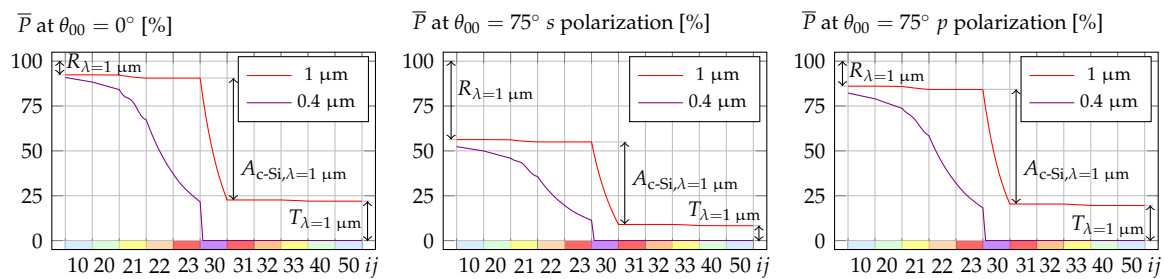
Figure 5. Irradiance depth profiles of the encapsulated bifacial HJ Si solar cell at the specified wavelengths, incident angles, and polarizations. Layers are denoted by their *ij* indexes and colors. They all have the same portion of *x* axis, regardless of their actual thickness (thick layers are shrunk, thin expanded).
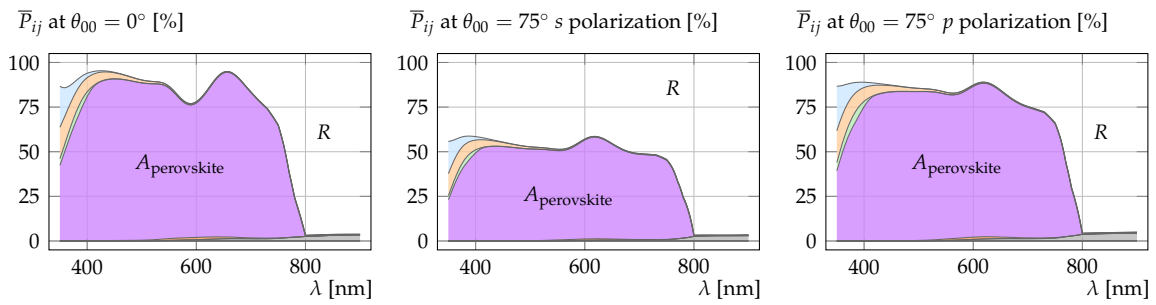
4.2. Perovskite Solar Cell

The second verification case is a perovskite ($CH_3NH_3PbI_3$) solar cell [29]. The device is deposited in inverted configuration on the bottom side of 1 mm glass superstrate. Its structure is depicted in Figure 6. The refractive indexes were obtained from [28].
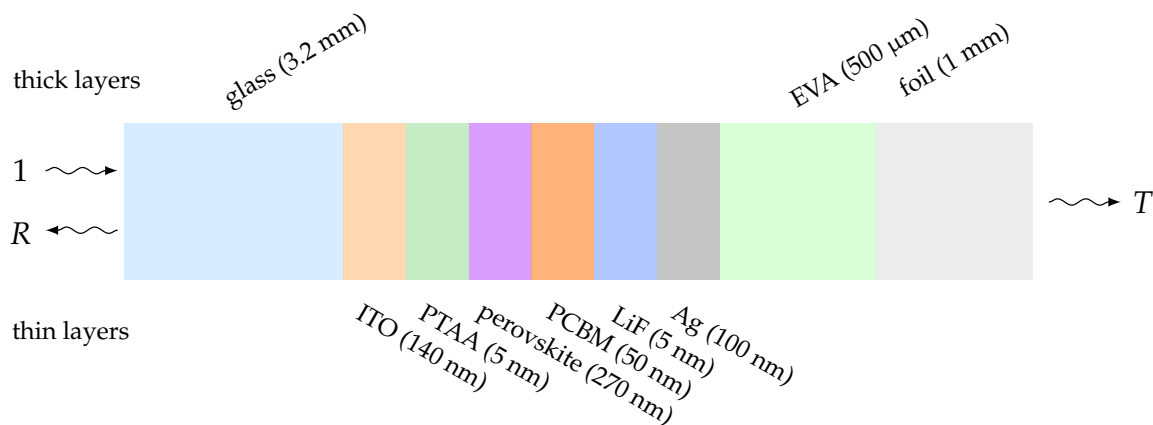

Figure 6. Perovskite solar cell multilayer structure.

The graphs in Figure 7 show PIM calculated wavelength dependent layer absorptances of the perovskite solar cell from Figure 6. The absorption distribution is as expected for the used structure. The perovskite absorber layer absorbs the major part of the ultraviolet and visible light ($A_{perovskite}$), and becomes transparent for the infrared light. The transmittance is zero because of the Ag layer at the bottom. The infrared light is therefore reflected, which is the opposite when the perovskite cell is used in a tandem solar cell as in [30]. The rear encapsulation layers (EVA and foil) also have no role in the simulation.

Figure 7. Wavelength dependent layer absorptances of the perovskite solar cell at the specified incident angles and polarizations. The height of a particular colored area (refer to Figure 6 for the meaning of the colors) represents the corresponding layer's absorptance as a function of wavelength. The white area above (up to 100%) represents the overall reflectance *R*.

The PIM calculated irradiance depth profiles of the perovskite cell are shown in Figure 8. To obtain finer curves, the profiles were calculated at forty additional depth points per layer. The irradiances at actual interfaces (marked by vertical grid lines in Figure 8) are identical to the ones that can be obtained from Figure 7 for the same wavelength $\lambda = 600$ nm.
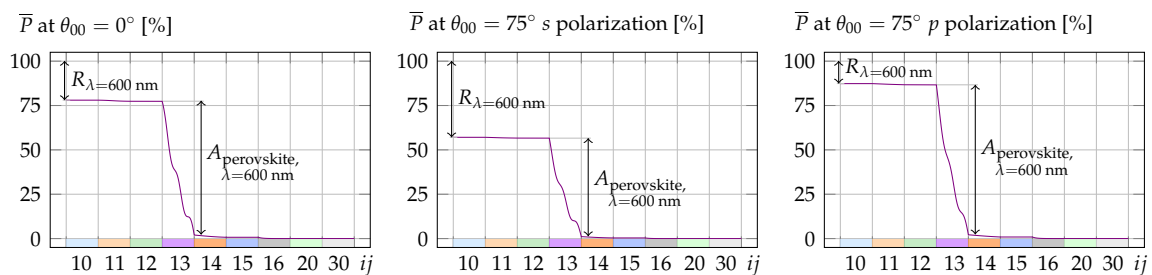
Figure 8. Irradiance depth profiles of the perovskite solar cell at the specified incident angles, polarizations, and $\lambda = 600$ nm. Layers are denoted by their ij indexes and colors. They all have the same portion of x axis, regardless of their actual thickness (thick layers are shrunk, thin expanded).
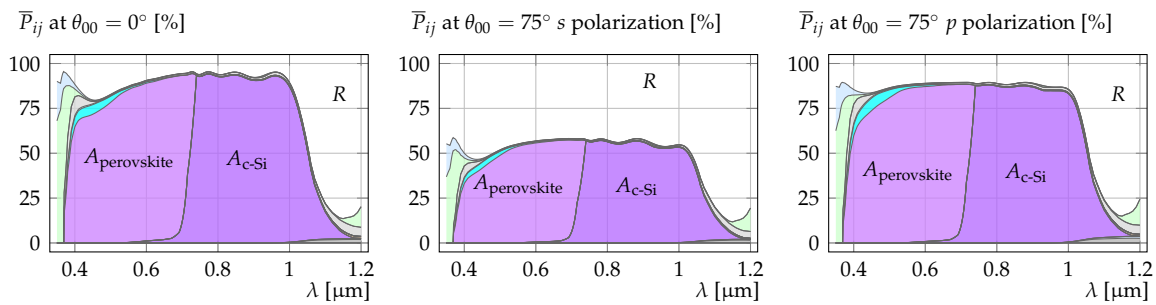
4.3. Perovskite/Silicon Tandem Solar Cell

The third verification case is a monolithic perovskite/silicon-heterojunction (SHJ) tandem solar cell [31] with structure depicted in Figure 9. The tandem cell consists of a rear emitter SHJ in inverted architecture and a p–i–n perovskite top cell.
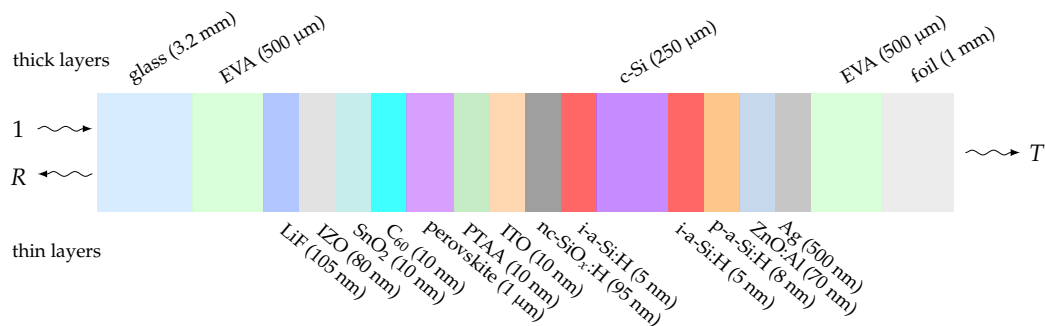
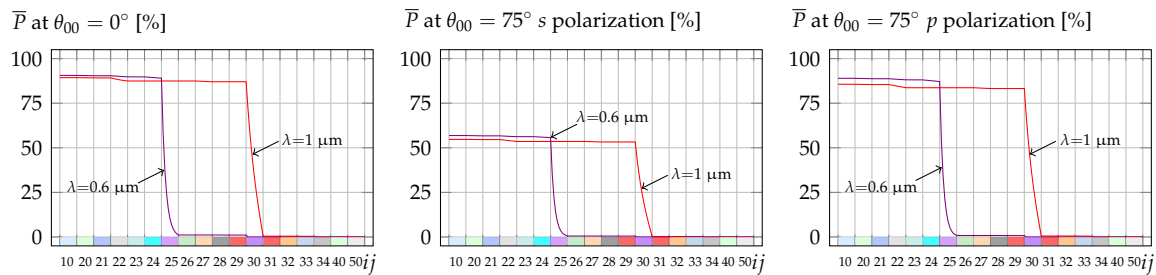**Figure 9.** Perovskite/SHJ tandem solar cell multilayer structure.

The graphs in Figure 10 show PIM calculated wavelength dependent layer absorptances of the perovskite/SHJ tandem solar cell from Figure 9. The absorption distribution is as expected. The perovskite absorber layer absorbs the ultraviolet and visible light ($A_{\text{perovskite}}$), while the c-Si

layer absorbs the infrared light ($A_{c\text{-}Si}$). The transmittance is zero because of the Ag layer. The rear encapsulation layers (EVA and foil) also have no role in the simulation.

Figure 10. Wavelength dependent layer absorptances of the perovskite/SHJ tandem solar cell at the specified incident angles and polarizations. The height of a particular colored area (refer to Figure 9 for the meaning of the colors) represents the corresponding layer's absorptance as a function of wavelength. The white area above (up to 100%) represents the overall reflectance R.

The PIM calculated irradiance depth profiles of the perovskite/SHJ tandem cell are shown in Figure 11. Each layer was divided into ten sublayers. The irradiances at actual interfaces (marked by vertical grid lines in Figure 11) are identical to the ones that can be obtained from Figure 10 for the same wavelengths.

Figure 11. Irradiance depth profiles of the perovskite/SHJ tandem solar cell at the specified wavelengths, incident angles, and polarizations. Layers are denoted by their ij indexes and colors. They all have the same portion of x axis, regardless of their actual thickness (thick layers are shrunk, thin expanded).

5. Potential Use of PIM in Gradient Optimization Procedures

To meet the design specifications, one can choose from a plethora of different optimization procedures. Using the proposed model, one can even employ a gradient optimization procedure (e.g., needle technique [32]), since it is possible to analytically obtain derivatives of PIM (Equations (20)–(23)). A few hints to obtain the necessary derivatives are gathered here:

$$\tilde{f} = \tilde{f}(d_{01}, d_{02} \ldots d_{0n_0}, d_{10}, d_{11}, d_{12} \ldots d_{1n_1} \ldots d_{m0}, d_{m1}, d_{m2} \ldots d_{mn_m}) \tag{24}$$

$$\frac{\partial}{\partial d_{xy}} \Re[\tilde{f}] = \Re\left[\frac{\partial \tilde{f}}{\partial d_{xy}}\right] \qquad \frac{\partial}{\partial d_{xy}} \Im[\tilde{f}] = \Im\left[\frac{\partial \tilde{f}}{\partial d_{xy}}\right] \tag{25}$$

$$\frac{\partial}{\partial d_{xy}} |\tilde{f}|^2 = 2\Re\left[\tilde{f}^* \frac{\partial \tilde{f}}{\partial d_{xy}}\right] \tag{26}$$

$$\frac{\partial}{\partial d_{iy}} \tilde{\mathbf{T}}_i^{(j)} = \begin{bmatrix} \frac{\partial \tilde{T}_{i11}^{(j)}}{\partial d_{iy}} & \frac{\partial \tilde{T}_{i12}^{(j)}}{\partial d_{iy}} \\ \frac{\partial \tilde{T}_{i21}^{(j)}}{\partial d_{iy}} & \frac{\partial \tilde{T}_{i22}^{(j)}}{\partial d_{iy}} \end{bmatrix} = \tilde{\mathbf{D}}_{i(j-1)}^{-1} \left(\prod_{l=j}^{y-1} \tilde{\mathbf{D}}_{il} \tilde{\mathbf{P}}_{il} \tilde{\mathbf{D}}_{il}^{-1}\right) \tilde{\mathbf{D}}_{iy} \frac{\partial \tilde{\mathbf{P}}_{iy}}{\partial d_{iy}} \tilde{\mathbf{D}}_{iy}^{-1} \left(\prod_{l=y+1}^{n_i} \tilde{\mathbf{D}}_{il} \tilde{\mathbf{P}}_{il} \tilde{\mathbf{D}}_{il}^{-1}\right) \tilde{\mathbf{D}}_{(i+1)0} \tag{27}$$

6. Conclusions

In this paper, we propose a new analytical Phase Integration Method (PIM) for irradiance calculation in a mixed structure containing an arbitrary number and ordering of coherent and incoherent layers. We develop a detailed mathematical derivation of the method, together with the algorithm to solve the resulting equations. The proposed method is based on subsequent phase integrations in incoherent layers, and is in fact a generalization of the well known GTMM. One of the immediate advantages of our method over the GTMM is that it enables us to obtain the irradiance depth profile in a straightforward manner. In addition, the PIM calculation consists of only basic algebraic operations between the intermediate GTMM transfer matrix elements, and therefore requires no significant additional computational cost. The mathematical model of the PIM is continuous and, because of coupled wave effects, without any interface energy imbalances. We verified the method equations against numerous cases, one of which is presented in this paper. Since we are able to analytically express the irradiance, it is also possible to obtain analytical layer thickness derivatives. Although the derivative expressions tend to be somewhat long and cumbersome, they are nevertheless analytical. Hence, the method requires no numerical derivation, thus making the PIM suitable for use with gradient optimization methods.

Abbreviations

TMM	Transfer-Matrix Method
TLM	Transmission Line Method
GTMM	General Transfer-Matrix Method
GTLM	Generalized Transmission Line Method
EMM	Equivalent Matrix Method
SAM	Spectral Averaging Method
SCM	Spectral Convolution Method
RTM	Random Thickness Method
RPM	Random Phase Method
ETAM	Equispaced Thickness Averaging Method
EPAM	Equispaced Phase Averaging Method
PEM	Phase Elimination Method
FEM	Finite Element Method
FDTD	Finite Difference Time Domain
RCWA	Rigorous Coupled Wave Analysis
PIM	Phase Integration Method
CROWM	combined ray optics/wave optics model
HJ Si	heterojunction silicon solar cell
EVA	ethylene-vinyl acetate
ITO	indium tin oxide
n-a-Si:H	n-type hydrogenated amorphous silicon
i-a-Si:H	intrinsic hydrogenated amorphous silicon
p-a-Si:H	p-type hydrogenated amorphous silicon

c-Si   n-type crystalline silicon
PTAA   polytriaryl amine
PCBM   phenyl-C61-butyric acid methyl ester
LiF   lithium fluoride
Ag   silver
SHJ   silicon-heterojunction
IZO   indium zinc oxide
SnO_2 tin oxide
nc-SiO_x:H   n-doped nanocrystalline silicon oxide

Appendix A

Expression for P_{ij} in Equation (18) can be transformed into

$$P_{ij} = P_{ij\Re} + P_{ij\Im}, \tag{A1}$$

where

$$P_{ij\Re} = \frac{\Re[\tilde{\eta}_{i(j-1)}](c_{i11b}^{(j)} \cos^2 \Re[\tilde{\delta}_{(i+1)0}] + c_{i12b}^{(j)} \cos \Re[\tilde{\delta}_{(i+1)0}] \sin \Re[\tilde{\delta}_{(i+1)0}] + c_{i13b}^{(j)} \sin^2 \Re[\tilde{\delta}_{(i+1)0}])}{\Re[\tilde{\eta}_0](c_{i21} \cos^2 \Re[\tilde{\delta}_{(i+1)0}] + c_{i22} \cos \Re[\tilde{\delta}_{(i+1)0}] \sin \Re[\tilde{\delta}_{(i+1)0}] + c_{i23} \sin^2 \Re[\tilde{\delta}_{(i+1)0}])} \tag{A2}$$

$$P_{ij\Im} = \frac{\Im[\tilde{\eta}_{i(j-1)}](c_{i11s}^{(j)} \cos^2 \Re[\tilde{\delta}_{(i+1)0}] + c_{i12s}^{(j)} \cos \Re[\tilde{\delta}_{(i+1)0}] \sin \Re[\tilde{\delta}_{(i+1)0}] + c_{i13s}^{(j)} \sin^2 \Re[\tilde{\delta}_{(i+1)0}])}{\Re[\tilde{\eta}_0](c_{i21} \cos^2 \Re[\tilde{\delta}_{(i+1)0}] + c_{i22} \cos \Re[\tilde{\delta}_{(i+1)0}] \sin \Re[\tilde{\delta}_{(i+1)0}] + c_{i23} \sin^2 \Re[\tilde{\delta}_{(i+1)0}])}, \tag{A3}$$

and the *c* constants are real:

$$c_{i11b}^{(j)} = |\tilde{T}_{i11}^{(j)} e^{-\Im[\tilde{\delta}_{(i+1)0}]} + \tilde{T}_{i12}^{(j)} \tilde{r}_{(i+1)0} e^{\Im[\tilde{\delta}_{(i+1)0}]}|^2 - |\tilde{T}_{i21}^{(j)} e^{-\Im[\tilde{\delta}_{(i+1)0}]} + \tilde{T}_{i22}^{(j)} \tilde{r}_{(i+1)0} e^{\Im[\tilde{\delta}_{(i+1)0}]}|^2 \tag{A4}$$

$$c_{i12b}^{(j)} = 4\Im[\tilde{r}_{(i+1)0}(\tilde{T}_{i11}^{(j)*} \tilde{T}_{i12}^{(j)} - \tilde{T}_{i21}^{(j)*} \tilde{T}_{i22}^{(j)})] \tag{A5}$$

$$c_{i13b}^{(j)} = |\tilde{T}_{i11}^{(j)} e^{-\Im[\tilde{\delta}_{(i+1)0}]} - \tilde{T}_{i12}^{(j)} \tilde{r}_{(i+1)0} e^{\Im[\tilde{\delta}_{(i+1)0}]}|^2 - |\tilde{T}_{i21}^{(j)} e^{-\Im[\tilde{\delta}_{(i+1)0}]} - \tilde{T}_{i22}^{(j)} \tilde{r}_{(i+1)0} e^{\Im[\tilde{\delta}_{(i+1)0}]}|^2 \tag{A6}$$

$$c_{i11s}^{(j)} = 2\Im[(\tilde{T}_{i21}^{(j)} e^{-\Im[\tilde{\delta}_{(i+1)0}]} + \tilde{T}_{i22}^{(j)} \tilde{r}_{(i+1)0} e^{\Im[\tilde{\delta}_{(i+1)0}]})(\tilde{T}_{i11}^{(j)*} e^{-\Im[\tilde{\delta}_{(i+1)0}]} + \tilde{T}_{i12}^{(j)*} \tilde{r}_{(i+1)0}^* e^{\Im[\tilde{\delta}_{(i+1)0}]})] \tag{A7}$$

$$c_{i12s}^{(j)} = 4\Re[\tilde{r}_{(i+1)0}(\tilde{T}_{i12}^{(j)} \tilde{T}_{i21}^{(j)*} - \tilde{T}_{i11}^{(j)*} \tilde{T}_{i22}^{(j)})] \tag{A8}$$

$$c_{i13s}^{(j)} = 2\Im[(\tilde{T}_{i21}^{(j)} e^{-\Im[\tilde{\delta}_{(i+1)0}]} - \tilde{T}_{i22}^{(j)} \tilde{r}_{(i+1)0} e^{\Im[\tilde{\delta}_{(i+1)0}]})(\tilde{T}_{i11}^{(j)*} e^{-\Im[\tilde{\delta}_{(i+1)0}]} - \tilde{T}_{i12}^{(j)*} \tilde{r}_{(i+1)0}^* e^{\Im[\tilde{\delta}_{(i+1)0}]})] \tag{A9}$$

$$c_{i21} = |\tilde{T}_{i11} e^{-\Im[\tilde{\delta}_{(i+1)0}]} + \tilde{T}_{i12} \tilde{r}_{(i+1)0} e^{\Im[\tilde{\delta}_{(i+1)0}]}|^2 \tag{A10}$$

$$c_{i22} = 4\Im[\tilde{T}_{i12} \tilde{r}_{(i+1)0} \tilde{T}_{i11}^*] \tag{A11}$$

$$c_{i23} = |\tilde{T}_{i11} e^{-\Im[\tilde{\delta}_{(i+1)0}]} - \tilde{T}_{i12} \tilde{r}_{(i+1)0} e^{\Im[\tilde{\delta}_{(i+1)0}]}|^2, \tag{A12}$$

and further, $\tilde{r}_{(i+1)0}$ is the complex reflection coefficient of the $(i + 1)0$th incoherent layer:

$$\tilde{r}_{(i+1)0} = \frac{\tilde{T}_{21}^{((i+1)1)}}{\tilde{T}_{11}^{((i+1)1)}}. \tag{A13}$$

The $\overline{P}_{ij}$ integral in Equation (19) transforms into sum of two integrals of type

$$\int_{-\frac{\pi}{2}}^{\frac{\pi}{2}} \frac{c_{11} \cos^2 x + c_{12} \cos x \sin x + c_{13} \sin^2 x}{c_{21} \cos^2 x + c_{22} \cos x \sin x + c_{23} \sin^2 x} dx = \int_{-\frac{\pi}{2}}^{\frac{\pi}{2}} \frac{c_{13} \tan^2 x + c_{12} \tan x + c_{11}}{c_{23} \tan^2 x + c_{22} \tan x + c_{21}} dx, \tag{A14}$$

where *c*s are real constants. The definite integral exists, if there are no zeros in the denominator, i.e. when the determinant is negative, $c_{22}^2 - 4c_{21}c_{23} < 0$. By setting $c_{21} = c_{i21}$, $c_{22} = c_{i22}$ and $c_{23} = c_{i23}$, one can obtain the determinant value:

$$4c_{i21}c_{i23} - c_{i22}^2 = 4c_{i21}c_{i23} - c_{i22}^2 = 4|\tilde{T}_{i11}|^4 e^{-4\Im[\tilde{\delta}_{(i+1)0}]} \left(1 - \frac{|\tilde{T}_{i12}|^2}{|\tilde{T}_{i11}|^2}|\tilde{r}_{(i+1)0}|^2 e^{4\Im[\tilde{\delta}_{(i+1)0}]}\right)^2 > 0. \quad \text{(A15)}$$

Note that $\frac{|\tilde{T}_{i12}|^2}{|\tilde{T}_{i11}|^2}$ is the reverse reflectance of the coherent stack between incoherent layers $(i+1)0$ and $i0$, $|\tilde{r}_{(i+1)0}|^2$ is the forward reflectance of the $(i+1)0$th incoherent layer, and $e^{4\Im[\tilde{\delta}_{(i+1)0}]}$ is the absorptance factor in the $(i+1)0$th layer. If the light is not trapped or amplified in the incoherent layer, then $\frac{|\tilde{T}_{i12}|^2}{|\tilde{T}_{i11}|^2}|\tilde{r}_{(i+1)0}|^2 e^{4\Im[\tilde{\delta}_{(i+1)0}]} < 1$, which is true for physically feasible structures. Since none of the other terms is zero, the integral exists. The integral in Equation (A14) is solved by introducing a new variable $u = \tan x$.

$$\lim_{\epsilon \to 0} \int_{\tan(-\frac{\pi}{2}+\epsilon)}^{\tan(\frac{\pi}{2}-\epsilon)} \frac{c_{13}u^2 + c_{12}u + c_{11}}{(u^2+1)(c_{23}u^2 + c_{22}u + c_{21})} du = \frac{(c_{13}-c_{11})(c_{23}-c_{21}) + c_{12}c_{22}}{(c_{23}-c_{21})^2 + c_{22}^2} +$$
$$+ \frac{c_{22}(c_{22}(c_{13}+c_{11}) - c_{12}(c_{23}+c_{21})) + 2(c_{23}-c_{21})(c_{11}c_{23}-c_{13}c_{21})}{((c_{23}-c_{21})^2 + c_{22}^2)\sqrt{4c_{21}c_{23}-c_{22}^2}} \quad \text{(A16)}$$

With the integral solved, by putting everything back together and doing some lengthly complex algebra, Equations (22) and (23) are obtained. The $\overline{T}_{i0}$ integral in Equation (19) is solved in the same way.

References

1. Knittl, Z. Optics of dielectric layers. In *Optics of Thin Films (An Optical Multilayer Theory)*; Ballard, S.S., Ed.; John Wiley & Sons: Hoboken, NJ, USA, 1976; pp. 35–68.
2. Born, M.; Wolf, E. Basic properties of the electromagnetic field. In *Principles of Optics: Electromagnetic Theory of Propagation, Interference and Diffraction of Light*; Cambridge University Press: Cambridge, UK, 2002; pp. 1–74.
3. Macleod, H.A. Basic theory. In *Thin-Film Optical Filters*; Pike, E.R., Brown, R.G.W., Eds.; CRC Press: Boca Raton, FL, USA, 2010; pp. 13–71.
4. Stathopoulos, N.A.; Palilis, L.C.; Savaidis, S.P.; Yesayan, S.R.; Vasilopoulou, M.; Papadimitropoulos, G.; Davazoglou, D.; Argitis, P. Optical Modeling of Hybrid Polymer Solar Cells Using a Transmission-Line Model and Comparison with Experimental Results. *IEEE J. Sel. Top. Quantum Electron.* **2010**, *16*, 1784–1791. [CrossRef]
5. Stathopoulos, N.A.; Palilis, L.C.; Yesayan, S.R.; Savaidis, S.P.; Vasilopoulou, M.; Argitis, P. A transmission line model for the optical simulation of multilayer structures and its application for oblique illumination of an organic solar cell with anisotropic extinction coefficient. *J. Appl. Phys.* **2011**, *110*, 114506. [CrossRef]
6. Donges, A. The coherence length of black-body radiation. *Eur. J. Phys.* **1998**, *19*, 245–249. [CrossRef]
7. Lee, W.; Lee, S.Y.; Kim, J.; Kim, S.C.; Lee, B. A numerical analysis of the effect of partially-coherent light in photovoltaic devices considering coherence length. *Opt. Express* **2012**, *20*, A941–A953. [CrossRef] [PubMed]
8. Pettersson, L.A.A.; Roman, L.S.; Inganäs, O. Modeling photocurrent action spectra of photovoltaic devices based on organic thin films. *J. Appl. Phys.* **1999**, *86*, 487–496. [CrossRef]
9. Peumans, P.; Yakimov, A.; Forrest, S.R. Small molecular weight organic thin-film photodetectors and solar cells. *J. Appl. Phys.* **2003**, *93*, 3693–3723. [CrossRef]
10. Kim, J.; Jung, S.; Jeong, I. Optical Modeling for Polarization-dependent Optical Power Dissipation of Thin-film Organic Solar Cells at Oblique Incidence. *J. Opt. Soc. Korea* **2012**, *16*, 6–12. [CrossRef]
11. Larouche, S.; Martinu, L. Openfilters: Open-source software for the design, optimization, and synthesis of optical filters. *Appl. Opt.* **2008**, *47*, C219–C230. [CrossRef]
12. Kang, K.; Lee, S.; Kim, J. Effect of an Incoherent Glass Substrate on the Absorption Efficiency of Organic Solar Cells at Oblique Incidence Analyzed by the Transfer Matrix Method with a Glass Factor. *Jpn. J. Appl. Phys.* **2013**, *52*, 052301. [CrossRef]
13. Mitsas, C.L.; Siapkas, D.I. Generalized matrix method for analysis of coherent and incoherent reflectance and transmittance of multilayer structures with rough surfaces, interfaces, and finite substrates. *Appl. Opt.* **1995**, *34*, 1678–1683. [CrossRef]

14. Katsidis, C.C.; Siapkas, D.I. General transfer-matrix method for optical multilayer systems with coherent, partially coherent, and incoherent interference. *Appl. Opt.* **2002**, *41*, 3978–3987. [CrossRef]

15. Stathopoulos, N.A.; Savaidis, S.P.; Botsialas, A.; Ioannidis, Z.C.; Georgiadou, D.G.; Vasilopoulou, M.; Pagiatakis, G. Reflection and transmission calculations in a multilayer structure with coherent, incoherent, and partially coherent interference, using the transmission line method. *Appl. Opt.* **2015**, *54*, 1492–1504. [CrossRef] [PubMed]

16. Centurioni, E. Generalized matrix method for calculation of internal light energy flux in mixed coherent and incoherent multilayers. *Appl. Opt.* **2005**, *44*, 7532–7539. [CrossRef]

17. Puhan, J.; Lipovšek, B.; Bűrmen, A.; Fajfar, I. An Accurate Representation of Incoherent Layers Within One-Dimensional Thin-Film Multilayer Structures With Equivalent Propagation Matrices. *IEEE Photonics J.* **2017**, *9*, 6501112. [CrossRef]

18. Sarrazin, M.; Herman, A.; Deparis, O. First-principle calculation of solar cell efficiency under incoherent illumination. *Opt. Express* **2013**, *21*, A616–A630. [CrossRef] [PubMed]

19. Prentice, J.S.C. Coherent, partially coherent and incoherent light absorption in thin-film multilayer structures. *J. Phys. D Appl. Phys.* **2000**, *33*, 3139–3145. [CrossRef]

20. Troparevsky, M.C.; Sabau, A.S.; Lupini, A.R.; Zhang, Z.Y. Transfer-matrix formalism for the calculation of optical response in multilayer systems: From coherent to incoherent interference. *Opt. Express* **2010**, *18*, 24715–24721. [CrossRef]

21. Kang, K.; Lee, S.; Kim, J.; Kim, S.; Han, Y.; Baek, S. A Simple Numerical Modeling of the Effect of the Incoherent Thick Substrate in Thin-Film Solar Cells Based on the Equispaced Thickness Method. *IEEE Photonics J.* **2016**, *8*, 8400312. [CrossRef]

22. Kang, K.; Kim, S.; Kim, J. Numerical modeling of the effect of multiple incoherent layers in Cu(In,Ga)Se-2 solar cells based on the equispaced thickness averaging method. *Appl. Opt.* **2018**, *57*, 2758–2765. [CrossRef]

23. Santbergen, R.; Smets, A.H.M.; Zeman, M. Optical model for multilayer structures with coherent, partly coherent and incoherent layers. *Opt. Express* **2013**, *21*, A262–A267. [CrossRef]

24. Čampa, A.; Krč, J.; Topič, M. Two Approaches for Incoherent Propagation of Light in Rigorous Numerical Simulations. *Prog. Electromagn. Res.* **2013**, *137*, 187–202. [CrossRef]

25. Lipovšek, B.; Čampa, A.; Guo, F.; Brabec, C.J.; Forberich, K.; Krč, J.; Topič, M. Detailed optical modelling and light-management of thin-film organic solar cells with consideration of small-area effects. *Opt. Express* **2017**, *25*, A176–A190. [CrossRef] [PubMed]

26. Lokar, Ž.; Lipovšek, B.; Razzaq, A.; Depauw, V.; Gordon, I.; Poortmans, J.; Krč, J.; Topič, M. Coupled modelling approach for optimization of bifacial silicon heterojunction solar cells with multi-scale interface textures. *Opt. Express* **2019**, *27*, A1554–A1568.

27. Lokar, Ž.; Lipovšek, B.; Topič, M.; Krč, J. Performance analysis of rigorous coupled-wave analysis and its integration in a coupled modeling approach for optical simulation of complete heterojunction silicon solar cells. *Beilstein J. Nanotechnol.* **2018**, *9*, 2315–2329. [CrossRef] [PubMed]

28. PhotoVoltaic Lighthouse Refractive Index Library. Available online: https://www.pvlighthouse.com.au/refractive-index-library (accessed on 18 June 2019).

29. Lipovšek, B.; Krč, J.; Topič, M. Microtextured Light-Management Foils and Their Optimization for Planar Organic and Perovskite Solar Cells. *IEEE J. Photovolt.* **2018**, *8*, 783–792. [CrossRef]

30. Bush, K.A.; Palmstrom, A.F.; Yu, Z.J.; Boccard, M.; Cheacharoen, R.; Mailoa, J.P.; McMeekin, D.P.; Hoye, R.L.Z.; Bailie, C.D.; Leijtens, T.; et al. 23.6%-efficient monolithic perovskite/silicon tandem solar cells with improved stability. *Nat. Energy* **2017**, *2*, 17009. [CrossRef]

31. Jošt, M.; Köhnen, E.; Morales-Vilches, A.B.; Lipovšek, B.; Jäger, K.; Macco, B.; Al-Ashouri, A.; Krč, J.; Korte, L.; Rech, B.; et al. Textured interfaces in monolithic perovskite/silicon tandem solar cells: advanced light management for improved efficiency and energy yield. *Energy Environ. Sci.* **2018**, *11*, 3511–3523. [CrossRef]

32. Tikhonravov, A.V.; Trubetskov, M.K.; DeBell, G.W. Optical coating design approaches based on the needle optimization technique. *Appl. Opt.* **2007**, *46*, 704–710. [CrossRef]